ARTICLE   OPEN

Polycrystalline morphology and mechanical strength of nanotube fibers

Nitant Gupta[1], Evgeni S. Penev[1] and Boris I. Yakobson [1 ✉]

Correlating mechanical performance with mesoscale structure is fundamental for the design and optimization of light and strong fibers (or any composites), most promising being those from carbon nanotubes. In all forms of nanotube fiber production strategies, due to tubes' mutual affinity, some degree of bundling into liquid crystal-like domains can be expected, causing heterogeneous load transfer within and outside these domains, and having a direct impact on the fiber strength. By employing large-scale coarse-grained simulations, we demonstrate that the strength s of nanotube fibers with characteristic domain size D scales as $s \sim 1/D$, while the degree of longitudinal/axial disorder within the domains (akin to a smectic $\leftrightarrow$ nematic phase transition) can substantially mitigate this dependence.

INTRODUCTION

Hierarchical design or natural assembly is ubiquitous in biological structural materials, from the classic examples of wood and bone/ collagen, to the super-tough and highly intriguing like spider-silk and nacre[1–4], which has inspired biomimetic attempts[5–7], eventually finding its way into nanomaterial-assemblies of graphene, boron-nitride[8,9], carbon, or inorganic nanotubes[10]. The carbon nanotubes (CNTs) are exceptionally promising to combine light-weight and strength[11] and have driven substantial development in scalable synthesis[12] and CNT-fiber spinning[13].

The strength s of parallel array-assemblies derives from the length of the constituents $\sim L$ and the traction at the interfaces, an effective force per length f, opposing the tubes slippage against each other, with $s \sim fL$[14]. This relationship holds well when axially tube positions are random, and most tubes touch laterally to all neighbors (i.e., 12 for a close packing). However, in fiber synthesis from tube solutions/suspensions[15–17], forests[18,19], or direct spinning from CVD growth[20–24], the tubes often form some a priori groups ('random tangles of bundled tubes'[25], or 'liquid crystalline domains'[26,27]) retained then in the fiber morphology. Some lateral contacts expand while others are lost, directly affecting the strength. The important goal of quantifying the morphology-strength relation in realistic fibers calls for (i) capturing the morphology in at least one measure, a transverse size (roughly a 'diameter') D of the grouped mesoscale domains, and then (ii) exploring how it affects the overall strength of the fiber.

In general, the notion of strength scaling with a domain size is rather common. In polycrystalline ductile materials like metals, there is the Hall–Petch relationship of strength and size of domains or grains, $s \sim 1/\sqrt{D}$ (due to dislocation slip restricted by the grain boundaries)[28]. A similar relation, albeit of different nature, was described for graphene[29]. In carbon fibers elastic moduli and strength dependence on the crystallite size has also been long noted empirically[30,31].

The origin of the a priori stacking in the aligned domains of tubes is due to long-range van der Waals attraction and high L/d ratio, which causes neighbors to not only align, but also maximize contact, to lower total surface energy. In models related to liquid crystalline phases[32], it has been shown that when rigid cylinders

with only repulsive (or sometimes weakly attractive[33]) interactions are concentrated together in a liquid medium, they undergo orientational alignment, to increase their translational entropy. If agglomeration into aligned clusters of n tubes is treated as a kinetic growth process, in the gas phase as an example, it occurs on a timescale $t \sim n/\beta c$ (c is the initial tube concentration and β is a collision kernel)[34]. Upon densification, these clusters become bundle-domains ('mesotubes') - and all assemble, positioned randomly along the fiber axis, giving it a characteristic polycrystalline morphology. The origin of fiber morphology is a rich subject, long observed and studied,[15,16,26,27,32,33] is far beyond our scope.

Our work aims to explore how a given morphology determines the mechanical strength of nanotube fibers, which has been a challenge not addressed, to the best of our knowledge. By using an expedient coarse-grained nanotube model, we quantify the strength of a mesoscale nanotube fiber as a function of the size D and degree of nanotube axial ordering in its constitutive bundles (with the number of nanotubes in a bundle varying over nearly 3 orders of magnitude). The ability to access such sub-micron model fiber sizes allows to demonstrate how the size $\leftrightarrow$ axial-ordering interplay determines the overall nanotube fiber strength.

RESULTS

Strength scaling in a bulk polycrystalline fiber

Load transfer across the ends of a nanotube fiber occurs through a continuous network of tube-tube interfaces. In the simple case of nanotube assemblies with perfect orientational alignment, nanotubes occupy a triangular lattice with their lateral neighbors as shown in Fig. 1a. When such fibers comprise domains formed by longitudinally aligned tubes of nearly equal length, the load transfer among the inter- and intra-domain interfaces are not identical. The former have tubes that straddle between axially adjacent tubes (Fig. 1a, left), forming bridges that can transmit load longitudinally[14,35]. However, in the latter case, the axial alignment of the gaps causes no tubes to straddle (Fig. 1a, right) and as a result, the top and bottom pieces are completely disconnected. Thus, in fibers composed of tubes with a narrow L-distribution, the load is transmitted almost solely across the inter-domain interfaces.

[1]Department of Materials Science and NanoEngineering, Rice University, Houston, TX 77005, USA. ✉email: biy@rice.edu
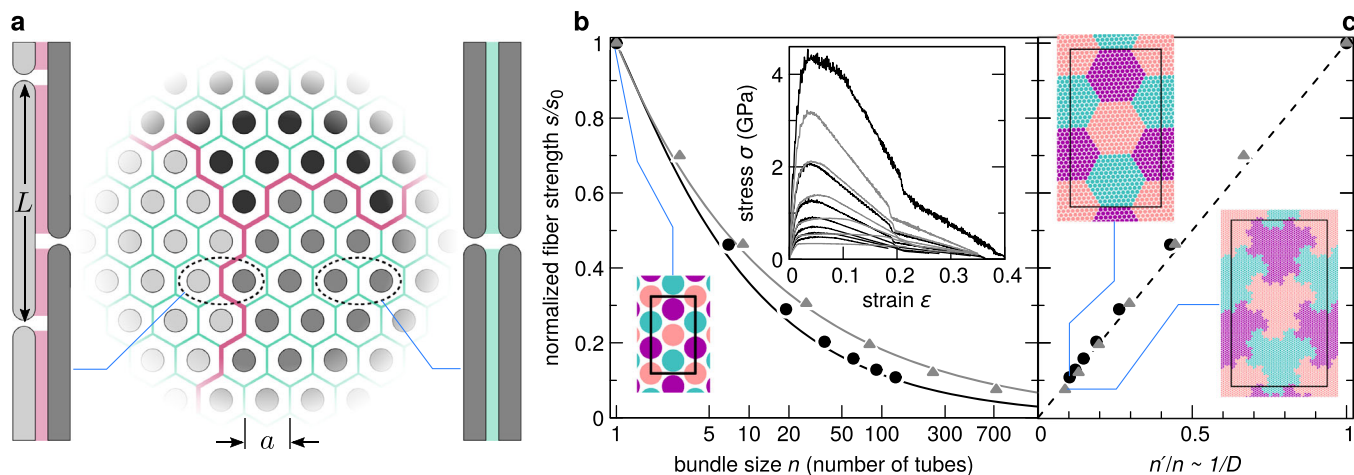
Fig. 1 Morphology and tensile behavior of a bulk fiber element. a Schematic representation of the domains or bundles (different shades of gray) viewed axially, demarcated by thicker lines which also represent the inter-domain interfaces. The thinner lines represent intra-domain interfaces. Each interface is represented by the edge of a tube's (hexagonal) Wigner--Seitz cell with length $a/\sqrt{3}$, where a is the inter-tube distance. The side cartoons show the axial arrangements of the encircled tubes: (left) inter-domain and (right) intra-domain interface. **b** Computed tensile strength of a representative fiber volume element as a function of the number of tubes (bundle size) in a constitutive domain for two domain shapes, shown in (**b**): hexagonal (circles) and fractal (triangles). The top-inset shows the respective stress-strain curves used to obtain s for each domain shape. The solid lines are the analytical fits $s(n)$ to the computed data points for the corresponding domain shapes (see Supplementary Note 2). Bottom-inset shows the unit cell for the domain-less ($n = 1$) fiber. **c** The same data points as in **b**, but plotted as a function of the periphery-to-bulk ratio $n'/n \sim 1/D$; the dashed line corresponds to $s/s_0 = n'/n$. Insets show cross-sectional views of the hexagonal and fractal systems, for their largest simulated bundle sizes: $n = 61$ and 729, respectively. The black rectangles denote the boundaries of the periodic cell. Tubes in the same domain/bundle are shown in the same color.

If n is the number of tubes in a domain, and n' is the number of inter-domain interfaces, then the total stress applied over the entire fiber cross-section gets redistributed to only the tubes near the domain interfaces, and the stress is effectively reduced by a factor of n'/n, the periphery-to-bulk ratio. The tubes will then slip, or fail at the interface, upon reaching the maximum load and the strength should behave as

$$s \sim \frac{n'}{n}\frac{fL}{d^2}. \tag{1}$$

Here, the assumption that assemblies of nanotubes will always fail preferentially at the interface and not by fracture of the tubes, stems from the weakness of the interface, i.e., when $fL/d^2 < s_{NT}$, as discussed in ref. [14]. This has been the consensus suggested by numerous state-of-the-art experiments[4,36–41], observing a linear relationship between the length of nanotubes and the strength of their fibers. However, if the interfaces could be strengthened to the point where they become at least as strong as the tubes ($fL/d^2 \geqslant s_{NT}$), the failure occurs due to tube fracture, bringing the strength of the fiber up to the intrinsic nanotube strength ($s \rightarrow s_{NT}$). In this case, the distinction between the inter- and intra-domain interfaces is lost, and the entire assembly shall behave as a continuum material, as is demonstrated later.

We show next that this scaling can be captured by a simple coarse-grained model[14] where all domains are identical and space-filling (for details, see the "Methods" section), allowing also for a quantitative understanding of the domain-size effect on the strength of bundles. The validity of Eq. (1) is also extended to the heterogeneity in the sizes of domains upon minor adjustments as discussed in Supplementary Note 3.

One unit cell consists of 6 domains, each of n tubes laterally, and 2 tubes in the axial z-direction separated by gaps. In addition, the nearest-neighbor domains are shifted axially by $\pm L/3$, mimicking a modified fcc arrangement[42]. A tri-color coding is used to identify tubes of identical z-position, and hence visually distinguish the domains as indicated in Fig. 1b, c. Primarily, the domains are chosen to have a hexagonal geometry (Fig. 1c, top-inset)

with n and n' determined by the number of hexagonal shells around a central tube. Additionally, to assess the effects of irregular-shaped domains[43], a fractal geometry (Fig. 1c, bottom-inset) is also adopted. Details about the geometry of domains is provided in Supplementary Note 2.

The computed fiber strength, Fig. 1b, displays a power-law dependence, $s \sim n^{-\alpha}$ (with $\alpha \simeq 1/2$ for hexagonal domains; see Supplementary Note 2). The inset shows the corresponding stress-strain curves for both domain shapes, demonstrating changes in fiber modulus Y as well as strength. It is interesting to note that fractal domains demonstrate a higher strength for the same n as compared to the hexagonal domains, suggesting that the domain shape-irregularity can contribute to a strengthening of the fibers. In Fig. 1c, s is plotted with respect to n'/n for both the domain shapes, with computed points following closely the $s/s_0 = n'/n$ line, where s_0 is the strength of the domain-less fiber ($n = 1$). In this regard, the ratio n'/n is the fundamental descriptor of strength scaling. Nonetheless, it may be more useful to relate strength to the domain size D which is perhaps easier to estimate or even measure through experiments. This is straightforward for regularly shaped domains where the perimeter is $\sim n'a$, the area is $\sim na^2$, and the area-to-perimeter ratio is equivalent to diameter, so that $D \sim na/n'$. Therefore, at least for regularly shaped domains, the fiber strength scales inversely with domain size, $s \sim 1/D$.

Finite-width fibers: modulus and strength scaling

In Fig. 2, the effect of domain size D for hexagonal shaped domains is explored for fibers of finite width (diameter $\simeq 18$ nm) and 0.6 µm periodic length, as shown in the top image (for details, see the Methods section). Here the stress-strain curves (not shown) follow a similar trend for both s and Y as in Fig. 1b, again exhibiting $s \sim 1/D$. So far, however, these trends are only applicable to very narrow length distributions. To generalize for wider length distributions or even polydisperse lengths, an axial disorder in the tube positions is introduced by applying a random shift δ_i for each tube i, as shown in Fig. 2b, c. These shifts represent the situation where tubes of different length assemble into domains with some length-wise alignment, however their ends
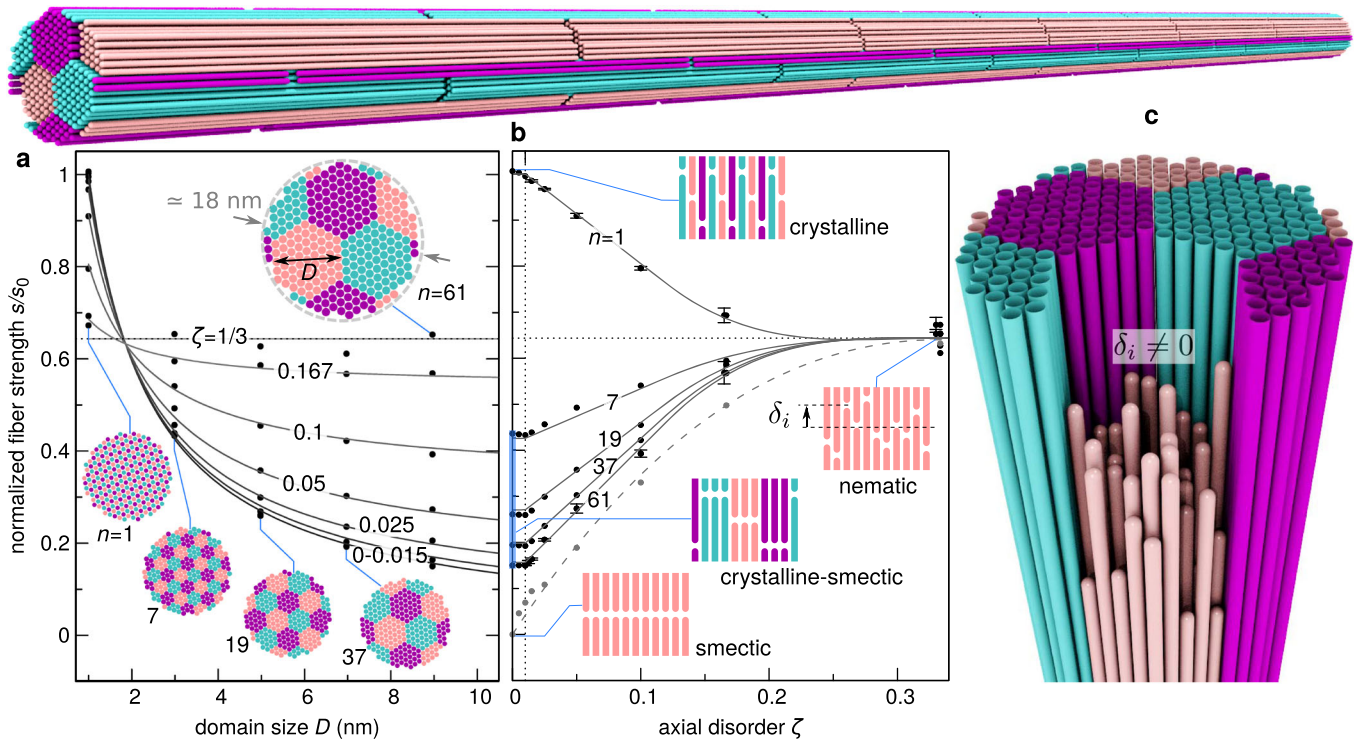
Fig. 2 Strength scaling in a finite-width fiber. a Computed fiber tensile strength (open circles) as a function of the domain size, $s(D)$. The inset illustrates the domains and fiber cross-sectional dimensions. The solid line shows the $1/D$-regression to the computed data points. **b** Fiber strength scaling with the axial disorder ζ. Error bars are provided for the $n = 1$ and $n = 61$, obtained from averaging over three random realizations for the same ζ. The solid lines in **a** and **b** are obtained by fitting the empirical relationship, $s(D, \zeta) = a(\zeta) + b(\zeta)/(D + c)$ to the computed data points, where $a(\zeta)$, $b(\zeta)$ are piecewise polynomial functions and c is a constant (see details in Supplementary Note 4). The dashed line in **b** represents the case where $n \to \infty$ or when one domain extends over the entire fiber width. **c** Perspective view of the fiber showing the brush-pattern interface due to the axial misalignment. The top image is a rendering of the entire simulated fiber for the case of largest domains ($n = 61$).

may no longer be perfectly aligned. In such a scenario, there can be some axial load transfer within the domain which is determined by the degree of axial disorder ζ, defined here as $\zeta \equiv \max(|\delta_i|/2L)$, with δ_i distributed uniformly. As a consequence, the $s \sim 1/D$ scaling, in Fig. 2a, is weighted by ζ, and eventually disappears completely as the axial disorder maximises. Therefore, ζ behaves like an 'order parameter' which tracks the transition from the highly ordered phase with $\zeta = 0$ to the phase when all tubes are axially delocalized ($\zeta \gtrsim 1/3$) inside the nanotube assembly.

The scaling of s and Y with D can be understood if one considers the assembly of very stiff tubes ($Y_{NT} \gg (f/u^*)(L/a)^2$; see Supplementary Note 5), which are connected by weak (van der Waals or sparsely-covalent) forces. Such an assembly will respond to an external axial stress σ by first yielding and failing at the interface which has the least stiffness or which is the most compliant. For a regularly shaped domain, the load transfer occurs through its exterior surface of area $n'aL \sim LD$ (because $n' \sim D/d$ and $a \sim d$). Moreover, taking into account the random shifts with $\delta \equiv \langle |\delta_i| \rangle$, the contact of individual (interior) tubes interlocked in a so-called brush-pattern[44] (shown in Fig. 2c) with the axially-adjacent domain, adds area $na\delta \sim \delta D^2/d$ (because $n \sim (D/d)^2$). Therefore, the tensile force $\sigma na^2 \sim \sigma D^2$ to the domain cross section is balanced by the traction, or shear stress τ times the total interface area: $\sigma D^2 \simeq \tau(LD + \delta D^2/d)$. For the linear-elastic response, τ is related to the interface friction f as $\tau \sim (f/u^*)(u/a) \sim (f/u^*)(u/d)$, where u is a small displacement between the rigid domain and its lateral neighbors, which at the critical failure point ($u = u^*$) becomes $\tau \sim f/d$. The strength is then obtained as

$$s = \sigma^* \sim f(L/Dd + \delta/d^2). \tag{2}$$

The modulus

$$Y = \sigma^*/\varepsilon^* \sim \frac{f}{u^*}\left(L^2/Dd + \delta L/d^2\right), \tag{3}$$

where $\varepsilon^* = u^*/L$, scales similarly as $1/D$ (or $\sim 1/d^2$, when δ is significant such that $\delta > Ld/D$), but is higher order in tube length $Y \sim L^2$ until it reaches the intrinsic value of the nanotube, $Y \to Y_{NT}$ (see Supplementary Note 5).

These analytical estimates are verified by the coarse-grained simulation results in Fig. 2b which plots the strength variation as a function of the axial disorder ζ for different n. For $\zeta \lesssim 0.01$, the strength $s = $ const, showcasing that the assumption of identical length tubes can explain even the strengths of fibers with narrow tube-length distributions. However, as the axial disorder increases, $0.01 \lesssim \zeta \lesssim 0.1$, a linear regime $s \sim \zeta$ is observed as the domains begin to lose their identity. The tubes in the interior of the domains can form stronger interfaces with their axial neighbors, and as a result an overall strengthening of the fiber occurs whenever $n > 1$. Further axial disorder increase, up to $\zeta \simeq 1/3$, for all n values leads to the same average configuration, and therefore s converges to a single value.

In contrast, for the domain-less fiber with no axial disorder, which are realized for $(n, \zeta) = (1, 0)$, the strength is the maximum because this case shows the best load transfer due to the fcc-like crystalline ordering of the tubes, as defined in ref. [14], which ensures the best possible overlap between every tube. This means that every interface is an inter-domain interface, and such a fiber will transmit load across the entire cross-section along the axial direction. In this case, any axial disorder $\zeta > 0$, reduces the perfect overlap arrangement and causes a reduction in strength until $\zeta \simeq 1/3$.
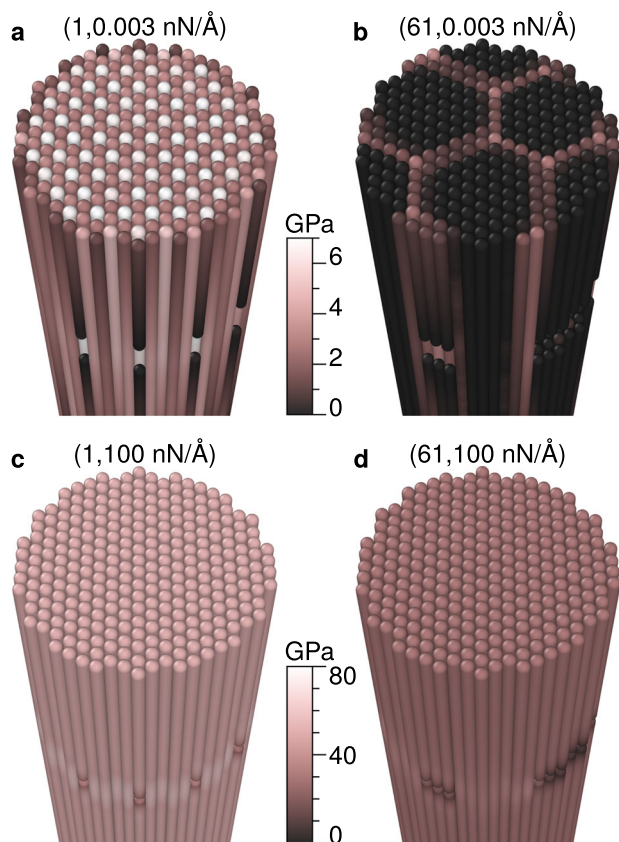
Fig. 3 **Stress distribution in a polycrystalline fiber for domains of perfectly aligned tubes ($\zeta = 0$).** Stress distribution in the fiber during tensile loading simulations right before critical failure for select combinations of size and friction (n, f), as indicated by the corresponding numerical values. Note that the colorbars for **a**, **b** and **c**, **d** have different ranges to make the stress distribution clearly visible.

One cannot but notice the apparent similarity between the nanotube fiber morphology as controlled by ζ and the common liquid-crystalline phases[45]. As illustrated in the insets in Fig. 2b, the axial ordering for $n \to \infty$ (truncated by the finiteness of the fiber itself) and $\zeta = 0$ can be associated with a smectic phase, and a nematic phase for $\zeta = 1/3$ and all n[46]. The modified fcc arrangement may then be categorized as a crystalline phase with $n = 1$ and $\zeta = 0$. Within such a description, the configurations with $n > 1$ and $\zeta = 0$, are hybrids between crystalline and smectic phases. The gray dashed curve in Fig. 2b, demonstrates the strength scaling of a pure smectic → nematic transition, where the strength of smectic configuration will truly be zero because the infinitely large domains are axially disconnected.

Figure 3 shows the stress distribution in the nanotubes of the finite-width fibers as they approach critical failure, i.e., maxima of the stress-strain curve. When the interface friction f is low enough, as in Fig. 3a, b, to allow tubes to slip upon critical failure, the patterns formed by the highly stressed tubes clearly distinguishes the domain-less fiber from the one with the largest domains, $n = 61$. Similar observations are also made for the representative volume elements of the bulk fibers with both hexagonal and fractal-shaped domains as discussed in Supplementary Note 1 and also Supplementary Figure 1. However, for very strong interfaces, $fL/d^2 \gg s_{NT}$, as demonstrated in Fig. 3c, d, the fiber will behave as a monolithic block with homogeneous stress distribution. In this case, upon reaching the maximum load, the tubes will break. The axial gaps act as local stress concentrators and their longitudinal alignment due to the formation of domains results in a large hole
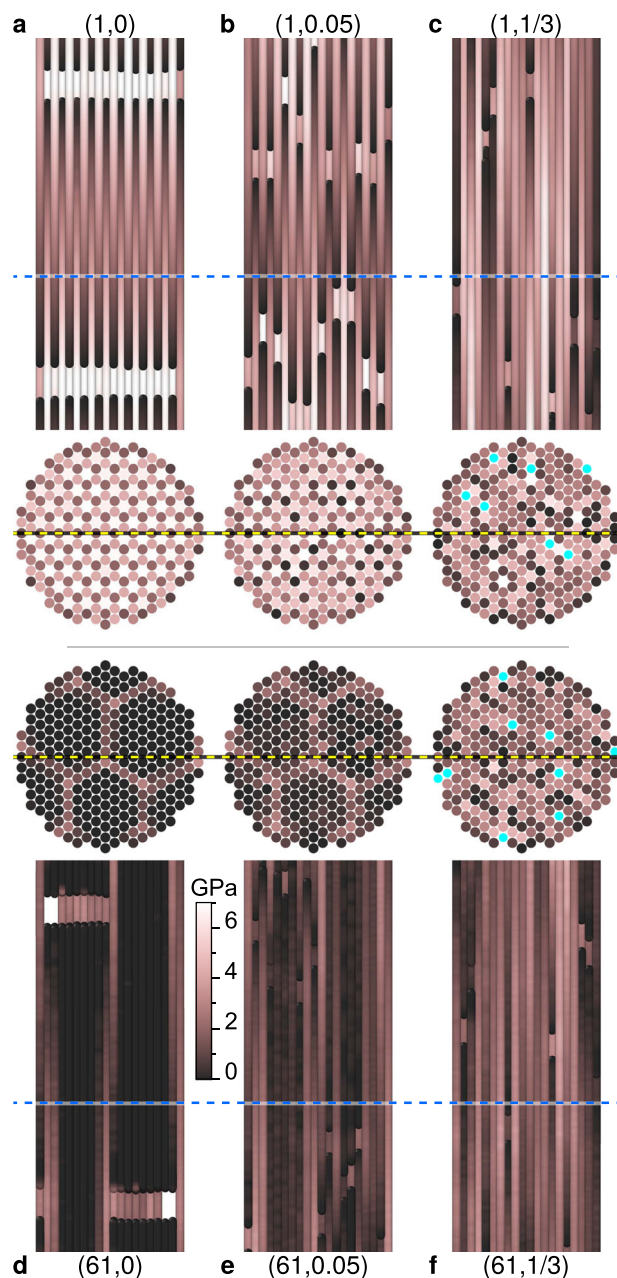

Fig. 4 **Simulated stress tomography of a finite-width fiber.** Longitudinal and transverse cross-sectional view of the finite-width fiber showing stress distribution during tensile loading simulations right before critical failure for select combinations of (n, ζ) as indicated by the corresponding numerical values. For each in (**a**–**f**), the dashed lines indicate the position of the respective cross section. The cyan filled circles represent gaps/holes in the fiber cross section.

of size D, comparable to the fiber cross section. These holes will have a larger stress concentration which leads to a lower strength of the fiber as indicated by the overall darker color in Fig. 3d. The fiber strength in these cases will be $s \sim s_{NT}/K$, where K is the stress concentration due to the gaps or holes. Interestingly, one can observe a similar trend in the stress distribution using continuum analysis, if nanotube fibers are modeled as anisotropic materials as detailed in Supplementary Note 6 and also Supplementary Fig. 5.

In Fig. 4 the stress distribution inside the nanotubes of finite-width fibers is shown along the longitudinal as well as transverse cross sections for different (n, ζ) values. Clearly, for $\zeta = 0$, Fig. 4a, d,

the regular arrangement of tubes results in a regular stress pattern. Most notable, however, are the hexagonal-shaped boundaries, also noticeable in Fig. 3b, outlined by the higher-stressed tubes along the periphery of the domains, as seen in the transverse cross section in Fig. 4d. Each such domain boundary surrounds tubes which are essentially load-free throughout their length. This further confirms that the tubes in the interior of the domains do not participate in appreciable load transfer along the axis of the bundle. A direct consequence of this is the observation that the maximum stress exhibited by constituent tubes in Fig. 4d never exceeds $\simeq 4$ GPa, while in Fig. 4a the maximum value approaches $\simeq 7$ GPa (lighter color), which also explains their corresponding fiber strengths.

With non-vanishing axial disorder, the regular stress patterns in Fig. 4a, d get slightly smeared out in Fig. 4b, e for $\zeta = 0.05$, and is completely smeared out in Fig. 4c, f, when $\zeta = 1/3$. As noted above, the two cases in Fig. 4c, f statistically represent the same configuration of the fiber but arrived at via different (n, ζ) paths, and therefore do not show significant difference in stress levels. These figures indicate that as the axial disorder increases, the domains start to lose their identity (gradually 'dissolve') and behave like a randomly shuffled arrangement of tubes. The tubes in the interior of the domains when $\zeta \ll 1/3$ are not completely load-free, but exhibit lower stress-levels than the tubes on the domain boundaries.

DISCUSSION

In summary, by employing an expedient coarse-grained model to access $\sim \mu m$ length scale, we demonstrate that when identical nanotubes in a fiber organize in D-sized domains, or bundles, with perfect end-to-end alignment, the fiber strength decreases as $s \sim 1/D$. This reduction in strength is shown to hold even for fibers comprising domains made from tubes of narrow length distribution. A similar scaling with the tube diameter d for domain-less bundles can be expected and is easily seen if domains are considered as 'mesotubes', which has been indeed proposed earlier, based on dimensional arguments, for nanotube aspect ratios L/d such that the strength is dominated by frictional load transfer[47].

Additionally, the uncovered trends point to possible strategies for strengthening of fibers, e.g., introduction of irregularities in domain shapes, which increases the periphery-to-bulk ratio n'/n. Another approach is to ensure higher degree of axial disorder when the tubes assemble into domains, which improves load transfer efficiency among axial neighbors. Therefore, highly polydisperse nanotube assemblies should, in principle, always have highly axially-misaligned domain configurations. The latter, upon proper densification to rule out large gaps between axially adjacent domains should demonstrate higher strength than the fibers with much narrower tube-length distributions. The multi-scale strength degradation due to the complex microstructure of nanotube fibers including the effects of voids/pores and entanglements of domains may be further explored by employing multi-level hierarchical modeling as was done, e.g., in ref. [48].

METHODS
Coarse-grained model and simulation details

All systems are represented using the coarse-grained model described in ref. [14] for a (5,5) CNT, without loss of generality. In the models for bulk and finite-width fibers, all tubes have identical length $L = 0.1$ μm, and the interface friction is set to $f = 0.003$ nN/Å, a combination chosen to effectively have strength ~ 4–5 GPa for the domainless fiber. The interface is described by a perfectly elasto-plastic constitutive relation, where the interface remains linear-elastic, i.e., $f(z, u < u^*) = (f/u^*) \cdot u$, up to a displacement $u = u^* \simeq 0.8$ nm, after which $f(z, u > u^*) \equiv f = const$. Here the difference between the function $f(z, u)$ and its value f should be noted, with z being the axial coordinate. In the

fiber models, periodic boundary conditions are imposed in each direction for the bulk, and along z-only for the finite-width. Each transverse lattice point (x, y) contains 2 (for bulk) or 6 (for finite-width) tubes per length, which leads to a z-period (box length) $\simeq 0.2$ μm and $\simeq 0.6$ μm, respectively. The cross-sectional area of a tube A_{NT} is defined as the area of the tube's hexagonal Wigner–Seitz cell in its closed-packed lattice with lattice constant a, $A_{NT} = \sqrt{3}a^2/2 \simeq 86$ Å^2, which is used consistently to define the axial stress and modulus of the tube. All tensile loading simulations are performed in LAMMPS[49] using the same protocol as in ref. [14].

REFERENCES

1. Kamat, S., Su, X., Ballarini, R. & Heuer, A. Structural basis for the fracture toughness of the shell of the conch *Strombus gigas*. *Nature* **405**, 1036–1040 (2000).
2. Sun, J. & Bhushan, B. Hierarchical structure and mechanical properties of nacre: a review. *RSC Adv.* **2**, 7617–7632 (2012).
3. Doblhofer, E., Heidebrecht, A. & Scheibel, T. To spin or not to spin: spider silk fibers and more. *Appl. Microbiol. Biotechnol.* **99**, 9361–9380 (2015).
4. Wei, X., Naraghi, M. & Espinosa, H. D. Optimal length scales emerging from shear load transfer in natural materials: application to carbon-based nanocomposite design. *ACS Nano* **6**, 2333–2344 (2012).
5. Bouville, F. et al. Strong, tough and stiff bioinspired ceramics from brittle constituents. *Nat. Mater.* **13**, 508–514 (2014).
6. Finnemore, A. et al. Biomimetic layer-by-layer assembly of artificial nacre. *Nat. Commun.* **3**, 1–6 (2012).
7. Rising, A. & Johansson, J. Toward spinning artificial spider silk. *Nat. Chem. Biol.* **11**, 309–315 (2015).
8. Kim, K. S. et al. Scalable manufacturing of boron nitride nanotubes and their assemblies: a review. *Semicond. Sci. Technol.* **32**, 013003 (2016).
9. McWilliams, A. D. S. et al. Surfactant-assisted individualization and dispersion of boron nitride nanotubes. *Nanoscale Adv.* **1**, 1096–1103 (2019).
10. Paineau, E. et al. A liquid-crystalline hexagonal columnar phase in highly-dilute suspensions of imogolite nanotubes. *Nat. Commun.* **7**, 1–8 (2016).
11. Siochi, E. J. & Harrison, J. S. Structural nanocomposites for aerospace applications. *MRS Bull.* **40**, 829–835 (2015).
12. Rao, R. et al. Carbon nanotubes and related nanomaterials: critical advances and challenges for synthesis toward mainstream commercial applications. *ACS Nano* **12**, 11756–11784 (2018).
13. Smail, F., Boies, A. & Windle, A. Direct spinning of CNT fibres: Past, present and future scale up. *Carbon* **152**, 218–232 (2019).
14. Gupta, N., Alred, J. M., Penev, E. S. & Yakobson, B. I. Universal strength scaling in carbon nanotube bundles with frictional load transfer. *ACS Nano* **15**, 1342–1350 (2021).
15. Liberman, L., Jamali, V., Pasquali, M. & Talmon, Y. Effect of carbon nanotube diameter and stiffness on their phase behavior in crowded solutions. *Langmuir* **36**, 242–249 (2019).
16. Jamali, V. et al. Enhanced ordering in length-polydisperse carbon nanotube solutions at high concentrations as revealed by small angle X-ray scattering. *Soft Matter* **17**, 5122–5130 (2021).
17. Headrick, R. J. et al. Structure-property relations in carbon nanotube fibers by downscaling solution processing. *Adv. Mater.* **30**, 1704482 (2018).
18. Dee, N. T. et al. In situ mechanochemical modulation of carbon nanotube forest growth. *Chem. Mater.* **31**, 407–418 (2018).
19. Hill, F. A., Havel, T. F., Hart, A. J. & Livermore, C. Enhancing the tensile properties of continuous millimeter-scale carbon nanotube fibers by densification. *ACS Appl. Mater. Interfaces* **5**, 7198–7207 (2013).
20. Li, Y.-L., Kinloch, I. A. & Windle, A. H. Direct spinning of carbon nanotube fibers from chemical vapor deposition synthesis. *Science* **304**, 276–278 (2004).
21. Vilatela, J. J. & Windle, A. H. Yarn-like carbon nanotube fibers. *Adv. Mater.* **22**, 4959–4963 (2010).
22. Lee, J. et al. Direct spinning and densification method for high-performance carbon nanotube fibers. *Nat. Commun.* **10**, 1–10 (2019).
23. Cho, H. et al. Effects of wet-pressing and cross-linking on the tensile properties of carbon nanotube fibers. *Materials* **11**, 2170 (2018).
24. Xu, W., Chen, Y., Zhan, H. & Wang, J. N. High-strength carbon nanotube film from improving alignment and densification. *Nano Lett.* **16**, 946–952 (2016).

25. Zhou, W. et al. Single wall carbon nanotube fibers extruded from super-acid suspensions: Preferred orientation, electrical, and thermal transport. *J. Appl. Phys.* **95**, 649–655 (2004).

26. Cho, S.-Y. et al. Continuous meter-scale synthesis of weavable tunicate cellulose/carbon nanotube fibers for high-performance wearable sensors. *ACS Nano* **13**, 9332–9341 (2019).

27. Park, K. T. et al. High-performance thermoelectric fabric based on a stitched carbon nanotube fiber. *ACS Appl. Mater. Interfaces* **13**, 6257–6264 (2021).

28. Anderson, P. M., Hirth, J. P. & Lothe, J. *Theory of Dislocations* (Cambridge University Press, New York, 2017).

29. Song, Z., Artyukhov, V. I., Yakobson, B. I. & Xu, Z. Pseudo Hall–Petch strength reduction in polycrystalline graphene. *Nano Lett.* **13**, 1829–1833 (2013).

30. Dresselhaus, M. S., Dresselhaus, G., Sugihara, K., Spain, I. L. & Goldberg, H. A. *Graphite fibers and filaments*, vol. 5 (Springer, Berlin, Heidelberg, 2013).

31. Kumar, S., Anderson, D. & Crasto, A. Carbon fibre compressive strength and its dependence on structure and morphology. *J. Mater. Sci.* **28**, 423–439 (1993).

32. De Gennes, P.-G. & Prost, J. *The Physics of Liquid Crystals* (Oxford University Press, Oxford, New York, 1993).

33. Green, M. J., Parra-Vasquez, A. N. G., Behabtu, N. & Pasquali, M. Modeling the phase behavior of polydisperse rigid rods with attractive interactions with applications to single-walled carbon nanotubes in superacids. *J. Chem. Phys.* **131**, 084901 (2009).

34. Boies, A. M. et al. Agglomeration dynamics of 1D materials: Gas-phase collision rates of nanotubes and nanorods. *Small* **15**, 1900520 (2019).

35. Wang, S., Lin, J., Xu, Z. & Xu, Z. Understanding macroscopic assemblies of carbon nanostructures with microstructural complexity. *Compos. - A: Appl. Sci. Manuf.* **143**, 106318 (2021).

36. Naraghi, M. et al. Atomistic investigation of load transfer between DWNT bundles "crosslinked" by PMMA oligomers. *Adv. Funct. Mater.* **23**, 1883–1892 (2013).

37. Tsentalovich, D. E. et al. Influence of carbon nanotube characteristics on macroscopic fiber properties. *ACS Appl. Mater. Interfaces* **9**, 36189–36198 (2017).

38. Vilatela, J. J., Elliott, J. A. & Windle, A. H. A model for the strength of yarn-like carbon nanotube fibers. *ACS Nano* **5**, 1921–1927 (2011).

39. Suekane, O., Nagataki, A., Mori, H. & Nakayama, Y. Static friction force of carbon nanotube surfaces. *Appl. Phys. Express* **1**, 064001 (2008).

40. Wang, C. et al. Tensile failure mechanisms of individual junctions assembled by two carbon nanotubes. *Compos. Sci. Technol.* **110**, 159–165 (2015).

41. Barber, A. H., Cohen, S. R., Eitan, A., Schadler, L. S. & Wagner, H. D. Fracture transitions at a carbon-nanotube/polymer interface. *Adv. Mater.* **18**, 83–87 (2006).

42. Xu, F., Xu, Z. & Yakobson, B. I. Site-percolation threshold of carbon nanotube fibers—fast inspection of percolation with Markov stochastic theory. *Phys. A* **407**, 341–349 (2014).

43. Pimenta, S. & Pinho, S. T. Hierarchical scaling law for the strength of composite fibre bundles. *J. Mech. Phys. Solids* **61**, 1337–1356 (2013).

44. Phoenix, S. L. & Beyerlein, I. J. Statistical strength theory for fibrous composite materials. In Kelly, A. & Zweben, C. (eds.) *Comprehensive Composite Materials*, 559-639 (Pergamon, Oxford, 2000).

45. Davis, V. A. Liquid crystalline assembly of nanocylinders. *J. Mater. Res.* **26**, 140–153 (2011).

46. Oswald, P. & Pieranski, P. *Smectic and columnar liquid crystals: concepts and physical properties illustrated by experiments*. (CRC Press, Boca Raton, 2005).

47. Yakobson, B., Samsonidze, G. & Samsonidze, G. Atomistic theory of mechanical relaxation in fullerene nanotubes. *Carbon* **38**, 1675–1680 (2000).

48. Gao, E., Lu, W. & Xu, Z. Strength loss of carbon nanotube fibers explained in a three-level hierarchical model. *Carbon* **138**, 134–142 (2018).

49. Thompson, A. P. et al. LAMMPS—a flexible simulation tool for particle-based materials modeling at the atomic, meso, and continuum scales. *Comput. Phys. Commun.* **271**, 108171 (2022).

ACKNOWLEDGEMENTS

AUTHOR CONTRIBUTIONS

B.I.Y. conceptualized the idea and provided supervision. N.G. and E.P. performed all simulations, analysis and visualization. All authors developed the methodology, and were involved in the writing of the original and the revised manuscript.

COMPETING INTERESTS

The authors declare no competing interests.

ADDITIONAL INFORMATION

Supplementary information The online version contains supplementary material available at https://doi.org/10.1038/s41524-022-00705-x.

Correspondence and requests for materials should be addressed to Boris I. Yakobson.

Reprints and permission information is available at http://www.nature.com/reprints

Publisher's note Springer Nature remains neutral with regard to jurisdictional claims in published maps and institutional affiliations.